

Time-delayed second-harmonic generation in cesium vapor

A. I. Lvovsky and S. R. Hartmann

Department of Physics, Columbia University, New York, New York 10027

(Received 24 April 1997)

Refined measurements and analysis of time-delayed second-harmonic generation on the $6D_{3/2}$ - $6S_{1/2}$ transition in Cs vapor are presented that resolve the disparity between the measured and calculated time delays reported in its initial observation. We extend our work to the $6D_{5/2}$ - $6S_{1/2}$ transition which, in agreement with our analysis, is characterized by a slightly smaller delay. For both transitions we also measure the amplitude of the second-harmonic intensity and find it close to what we estimate it should be. [S1050-2947(97)08611-3]

PACS number(s): 42.65.Ky, 42.50.Md

I. INTRODUCTION

Sum and difference frequency radiation generally appears simultaneously with the excitation fields that induce it. Until recently [1], this notion had not been examined in any detail. In many situations the notion of an immediate response is real [2], in other cases only apparent. A case in point is found in the experiments performed in an atomic vapor where a transverse magnetic field was applied to break symmetry [3,4]. Those experiments were performed using excitation pulses and detectors that worked in the nanosecond regime and were therefore just under the threshold of being able to resolve the noninstantaneous character of the response. By using picosecond excitation pulses, fast avalanche detectors, and working in a vapor of cesium whose heavy atoms retard the action of Doppler dephasing, the delay of the second-harmonic radiation recently has been made manifest [1]. A puzzling feature was that the magnitude of the delay seemed to be more than a factor of 2 greater than calculated [1]. This discrepancy raised questions as to the validity of the time-delay observation that we address in this paper. To this purpose we also report time-delay measurements of second-harmonic generation on the neighboring $6D_{5/2}$ - $6S_{1/2}$ transition and supplement them with quantitative measurements of the second-harmonic pulse energy.

Second-harmonic generation occurs when an optical excitation at frequency ω produces cooperative emission at 2ω . However, the process by which the second-harmonic radiation develops is best understood by examining the radiation distribution pattern of an isolated atom that has been put in a superposition state by the action of a short two-photon-resonant excitation pulse. For our system this pattern initially has a null in the phased-matched direction defined by and collinear with the excitation pulse. The application of a transverse magnetic field causes this pattern to change and develop a component in the phase-matched direction [5].

We begin by calculating the temporal evolution of the radiation pattern and displaying it pictorially. Our calculation also gives the second-harmonic pulse energy along the phase-matched direction, which is what we measure experimentally. These measurements, using sample cells of glass, are then described in detail. The metal (stainless-steel) cells used earlier produced eddy currents when subject to the pulsed (but static on the time scale of the experiment) magnetic field. These eddy currents were responsible in large

measure for the reported [1] discrepancy in second-harmonic delay. Significant corrections are also made by taking into account the temporal response of the detector.

Simultaneous with the second-harmonic generation are superfluorescence processes that modify the second-harmonic output. These too are delayed, but the relevant mechanisms are different and competing effects could be untangled. The trick was to generate the second-harmonic with excitation pulses that were not excessively energetic. In most cases second-harmonic signals could then be observed before or in the absence of any superfluorescence degradation. To this end we established the regime over which the second-harmonic intensity varied as the square of the excitation pulse intensity and beyond which it saturated. These measurements also enabled us to set a limit on the *area* (integrated Rabi frequency) of the excitation pulse to allow a quantitative check on the measured energy of the second-harmonic signal.

II. TEMPORAL EVOLUTION OF RADIATION PATTERN FOR AN ISOLATED ATOM

A. Formula development

A superposition state giving rise to a quadrupole moment $\langle \vec{Q} \rangle = e \langle 3\vec{r}\vec{r} - r^2\vec{I} \rangle$ radiates from the origin to \vec{R} with an intensity (Poynting's vector)

$$\vec{S}_0(\hat{n}) = \frac{ck^6}{144\pi R^2} |(\vec{I} - \hat{n}\hat{n}) \cdot \langle \vec{Q} \rangle \cdot \hat{n}|_{avg}^2 \hat{n}, \quad (2.1)$$

where \vec{I} is the identity operator, $\hat{n} = \vec{R}/R$, c is the velocity of light, $k = 2\pi/\lambda$, where λ is the quadrupole transition wavelength, and *avg* denotes an average over optical periods [6].

Boldface is used to indicate an operator. We calculate \vec{Q} from

$$\langle \vec{Q} \rangle = \text{Tr } \vec{Q} \rho, \quad (2.2)$$

where ρ is the density matrix, and decompose \vec{Q} according to

$$\vec{Q} = \sum_{q=-2}^{q=+2} \mathbf{Q}^{2,q} \vec{K}_q, \quad (2.3)$$

where $\mathbf{Q}^{2,q} = e\sqrt{16/\pi}Y^{2,q}(\hat{\mathbf{r}})$ is the q th element of a second-rank irreducible quadrupole tensor [$Y^{2,q}(\hat{\mathbf{r}})$ is a second-order solid harmonic] and the \vec{K}_q 's are defined by the relation $\hat{n} \cdot \vec{K}_q \cdot \hat{n} = \sqrt{4\pi/5}Y^{2,q}(\hat{n})$. They are given explicitly by

$$\vec{K}_{\pm 2} = \frac{1}{2} \sqrt{\frac{3}{2}} [\hat{1}\hat{1} - \hat{2}\hat{2} \pm i(\hat{1}\hat{2} + \hat{2}\hat{1})], \quad (2.4)$$

$$\vec{K}_{\pm 1} = \mp \frac{1}{2} \sqrt{\frac{3}{2}} [3\hat{1}\hat{1} + \hat{1}\hat{3} \pm i(\hat{3}\hat{2} + \hat{2}\hat{3})], \quad (2.5)$$

$$\vec{K}_0 = \left[\hat{3}\hat{3} - \frac{1}{2} \hat{1}\hat{1} - \frac{1}{2} \hat{2}\hat{2} \right]. \quad (2.6)$$

Writing \mathbf{R} for the response to the laser excitation pulse, \mathbf{H} for the Hamiltonian, and ρ_0 for the initial density matrix, ρ develops in time as

$$\rho = e^{-(i/\hbar)\mathbf{H}\mathbf{R}\rho_0\mathbf{R}^{-1}} e^{+(i/\hbar)\mathbf{H}\mathbf{R}}. \quad (2.7)$$

We specialize to $\hat{H} \perp (\hat{\mathbf{e}} \perp \hat{\mathbf{k}})$ and set $\hat{1} = \hat{H}$, $\hat{2} = \hat{\mathbf{k}}$, and $\hat{3} = \hat{\mathbf{e}}$ as unit vectors along the applied magnetic-field, propagation, and electric-field polarization directions, respectively. Since the dipole transition matrix elements associated with the $6S_{1/2}$ - $6P_{1/2}$ and $6P_{1/2}$ - $6D_{3/2,5/2}$ transitions are approximately (to within 20%) equal, we can characterize the two-photon resonant laser excitation pulse by an area Θ so that

$$\begin{aligned} & \langle D_{\hat{3}}, m'_J, m'_I | \mathbf{R} | S_{\hat{3}}, m_J, m_I \rangle \\ & \cong i \delta_{m'_J m_J} \delta_{m'_I m_I} (2m_J)^{(5/2-J_D)} \sin \Theta/2 \end{aligned}$$

and

$$\langle S_{\hat{3}}, m'_J, m'_I | \mathbf{R} | S_{\hat{3}}, m_J, m_I \rangle \cong \delta_{m'_J m_J} \delta_{m'_I m_I} \cos \Theta/2,$$

with $m_J = \pm \frac{1}{2}$ [7]. Here $J_D = 3/2, 5/2$ according to which $D_{3/2,5/2}$ state we refer and the subscript $\hat{3}$ denotes the quantization axis. The factor $(2m_J)^{(5/2-J_D)}$ comes from parity conservation. It then follows that

$$\langle \vec{\mathbf{Q}} \rangle = \vec{Q}_{SD} + \vec{Q}_{SD}^*, \quad (2.8)$$

where

$$\begin{aligned} \vec{Q}_{SD} &= i e^{-i(\Omega_D - \Omega_S)t} \frac{\rho_0 \sin \Theta}{2} \\ & \times \sum_{m_J = -1/2}^{+1/2} (2m_J)^{(5/2-J_D)} \\ & \times \sum_{m_I = -I}^{+I} \langle S_{\hat{3}}, m_J, m_I | e^{+(i/\hbar)\mathbf{H}_{int}t} \vec{\mathbf{Q}} \\ & \times e^{-(i/\hbar)\mathbf{H}_{int}t} | D_{\hat{3}}, m_J, m_I \rangle, \end{aligned} \quad (2.9)$$

where $\Omega_D - \Omega_S$ is the optical frequency of the quadrupole transition and \mathbf{H}_{int} contains the magnetic and hyperfine interactions.

Over the range of magnetic fields used in our experiments the Zeeman splittings were of the order of 1 GHz. The hyperfine interaction, on the other hand, splits the ground $6S_{1/2}$ state [8] by 9.2 GHz and the excited $6D_{3/2,5/2}$ states by about 0.1 GHz [9,10]. Since the latter splitting is small compared to the inverse Doppler width, we can neglect it without introducing any significant errors. In dealing with the $6S_{1/2}$ state we note that the $I=7/2$ nuclear spin leads to angular-momentum states characterized by $F=3,4$ with energies that we write as $\hbar\Omega_{S_3}$ and $\hbar\Omega_{S_4}$. Zeeman splitting occurs separately on each of these states and is thus a perturbation of the already existing hyperfine structure. We denote the Zeeman frequencies by ω with the appropriate angular-momentum subscripts. Then

$$\begin{aligned} \mathbf{H}_{int} &= \sum_{m_J = -J_D}^{J_D} m_J \hbar \omega_{J_D} | D_{\hat{1}}, J, m_J \rangle \langle D_{\hat{1}}, J, m_J | \\ & + \sum_{F=3}^4 \sum_{m_F = -F}^F [m_F \hbar \omega_{S_F} + \hbar(\Omega_{S_F} - \Omega_S)] | S_{\hat{1}}, F, m_F \rangle \\ & \times \langle S_{\hat{1}}, F, m_F |. \end{aligned} \quad (2.10)$$

The Zeeman splitting frequencies associated with the above Hamiltonian are $\omega_{3/2} = \frac{4}{5} \Omega_L$, $\omega_{5/2} = \frac{6}{5} \Omega_L$ for the $6D_{3/2,5/2}$ levels, respectively, and $\omega_{S_F} = (-1)^F \omega_{1/2}$ with $\omega_{1/2} = \frac{1}{4} \Omega_L$ for the $6S_{1/2}$ level, where Ω_L is the Larmor frequency of a free electron in the magnetic field H . Assuming that all hyperfine states are initially equally populated $\langle S_{\hat{3}}, m'_J, m'_I | \rho_0 | S_{\hat{3}}, m'_J, m'_I \rangle \equiv \rho_0 = 1/(2S+1)(2I+1) = \frac{1}{16}$ we resolve Eq. (2.9) as

$$\vec{Q}_{SD} = \sum_{q=-2}^{+2} Q_{SD}^{2,q} \vec{K}_q, \quad (2.11)$$

$$Q_{SD}^{2,q} = e^{-i\Omega_D t} \frac{\rho_0 \sin \Theta}{2} Q_0 \sum_{F=3}^4 e^{+i\Omega_{S_F} t} M(J_D, F, q, t), \quad (2.12)$$

where $Q_0 = \langle S || Q || D \rangle$ is the reduced quadrupole matrix element and

$$\begin{aligned} M(J_D, F, q, t) &= \sum_{m_J, m'_J = -1/2}^{+1/2} \sum_{m_I = -I}^{+I} (2m_J)^{(5/2-J_D)} \\ & \times T(F, m_J, m'_J) U(J_D, q, m'_J, m_J), \end{aligned} \quad (2.13)$$

$$\begin{aligned} T(F, m_J, m'_J) &= \sum_{m''_J = -1/2}^{1/2} \langle S_{\hat{3}}, m_J, m_I | S_{\hat{1}}, m''_J, m_I \rangle \\ & \times \langle S_{\hat{1}}, m''_J, m_I | S_{\hat{1}}, F, m_F \rangle e^{+im_F \omega_{S_F} t} \\ & \times \langle S_{\hat{1}}, F, m_F | S_{\hat{1}}, m''_J, m_I \rangle \\ & \times \langle S_{\hat{1}}, m''_J, m_I | S_{\hat{3}}, m'_J, m_I \rangle, \end{aligned} \quad (2.14)$$

$$U(J_D, q, m'_J, m_J) = \sum_{m''_J = -J_D}^{J_D} \langle S_{\hat{z}}, m'_J, m_J | \mathbf{q}^{2,q} | D_{\hat{z}}, m''_J, m_J \rangle \\ \times \langle D_{\hat{z}}, m''_J, m_J | e^{-i\omega_D \mathbf{J}_1 t} | D_{\hat{z}}, m_J, m_J \rangle, \quad (2.15)$$

and $\mathbf{q}^{2,q} = \mathbf{Q}^{2,q}/Q_0$ is the normalized quadrupole moment whose matrix elements are determined via the Wigner-Eckart theorem.

The intensity (2.1) then becomes

$$\vec{S}_0(\hat{n}) = S_0(\hat{n})\hat{n} = S(J_D, t, \theta, \phi)\hat{n}, \quad (2.16)$$

$$S(J_D, t, \theta, \phi) = \frac{ck^6}{72\pi R^2} Q_0^2 \left(\frac{\rho_0 \sin \Theta}{2} \right)^2 \\ \times \sum_{F=3}^4 \left| \sum_{q=0}^2 [M(J_D, F, q, t) \vec{W}_q(\hat{n})] \right|^2, \quad (2.17)$$

$$\vec{W}_q(\hat{n}) = (\vec{I} - \hat{n}\hat{n}) \cdot \frac{(\vec{K}_q + \vec{K}_{-q})}{(1 + \delta_{q0})} \cdot \hat{n}, \quad (2.18)$$

where the direction of \hat{n} is defined by polar angles θ and ϕ .

In Eq. (2.17) we have used $\langle \vec{\mathbf{Q}} \rangle_{avg}^2 = 2|\vec{Q}_{SD}|^2$ and $M(J_D, F, q, t) = M(J_D, F, -q, t)$. Since the detector used in the experiment was unable to resolve the 9.2-GHz beats associated with the $6S_{1/2}$ state splitting we have averaged the intensity (2.17) over one beat period by placing the sum over F before squaring. The \vec{W}_q 's are given explicitly by

$$\vec{W}_0(\hat{n}) = -\frac{3}{4} \sin(2\theta) \hat{\theta}, \quad (2.19)$$

$$\vec{W}_1(\hat{n}) = -\sqrt{\frac{3}{2}} i [\sin \phi \cos(2\theta) \hat{\theta} + \cos \phi \cos \theta \hat{\phi}], \quad (2.20)$$

$$\vec{W}_2(\hat{n}) = \sqrt{\frac{3}{2}} [\cos(2\phi) \cos \theta \hat{\theta} - \sin(2\phi) \hat{\phi}] \sin \theta, \quad (2.21)$$

while for $J_D = 3/2$ the M 's are given by

$$M\left(\frac{3}{2}, F, 0, t\right) = -\frac{1}{2\sqrt{5}} \left[\left(\cos \frac{1}{2} \omega_{3/2} t + 3 \cos \frac{3}{2} \omega_{3/2} t \right) T_s(F, t) \right. \\ \left. + \left(\sin \frac{1}{2} \omega_{3/2} t - 3 \sin \frac{3}{2} \omega_{3/2} t \right) T_n(F, t) \right], \quad (2.22)$$

$$M\left(\frac{3}{2}, F, 1, t\right) = -i \sqrt{\frac{3}{10}} \left(\sin \frac{3}{2} \omega_{3/2} t T_s(F, t) \right. \\ \left. + \cos \frac{3}{2} \omega_{3/2} t T_n(F, t) \right), \quad (2.23)$$

$$M\left(\frac{3}{2}, F, 2, t\right) = \sqrt{\frac{3}{10}} \sin \omega_{3/2} t \left(\sin \frac{1}{2} \omega_{3/2} t T_s(F, t) \right. \\ \left. + \cos \frac{1}{2} \omega_{3/2} t T_n(F, t) \right), \quad (2.24)$$

where we have defined

$$T_s(F, t) \equiv \frac{1}{2} + \sum_{m_F=1}^F \cos(m_F \omega_{1/2} t) = \frac{\sin\left[\frac{1}{2}(2F+1)\omega_{1/2} t\right]}{2 \sin\left(\frac{1}{2}\omega_{1/2} t\right)}, \quad (2.25)$$

$$T_n(F, t) \equiv \frac{1}{4} \sum_{m_F=1}^F m_F \sin(m_F \omega_{1/2} t) \\ = \frac{(1+F) \sin(F\omega_{1/2} t) - F \sin[(F+1)\omega_{1/2} t]}{16 \sin^2\left(\frac{1}{2}\omega_{1/2} t\right)}. \quad (2.26)$$

For $J_D = 5/2$

$$M\left(\frac{5}{2}, F, 0, t\right) = \frac{1}{4\sqrt{5}} \left[\left(2 \cos \frac{1}{2} \omega_{5/2} t + \cos \frac{3}{2} \omega_{5/2} t \right. \right. \\ \left. \left. + 5 \cos \frac{5}{2} \omega_{5/2} t \right) T_s(F, t) + \left(2 \sin \frac{1}{2} \omega_{5/2} t \right. \right. \\ \left. \left. - \sin \frac{3}{2} \omega_{5/2} t + 5 \sin \frac{5}{2} \omega_{5/2} t \right) T_n(F, t) \right], \quad (2.27)$$

$$M\left(\frac{5}{2}, F, 1, t\right) = \frac{i}{2\sqrt{30}} \left[\left(\sin \frac{3}{2} \omega_{5/2} t + 5 \sin \frac{5}{2} \omega_{5/2} t \right) T_s(F, t) \right. \\ \left. + \left(\cos \frac{3}{2} \omega_{5/2} t - 5 \cos \frac{5}{2} \omega_{5/2} t \right) T_n(F, t) \right], \quad (2.28)$$

$$M\left(\frac{5}{2}, F, 2, t\right) = -\frac{1}{2\sqrt{30}} \sin \omega_{5/2} t \left[\left(\sin \frac{1}{2} \omega_{5/2} t \right. \right. \\ \left. \left. + 5 \sin \frac{3}{2} \omega_{5/2} t \right) T_s(F, t) + \left(\cos \frac{1}{2} \omega_{5/2} t \right. \right. \\ \left. \left. - 5 \cos \frac{3}{2} \omega_{5/2} t \right) T_n(F, t) \right]. \quad (2.29)$$

The above formulas allow us to calculate the radiation distribution pattern from an isolated atom. We note that at $t = 0$, $T_n(F, t) = 0$ and so only the $M(J_D, F, q = 0, t)$'s are non-zero. But these terms are associated with $\vec{W}_0(\hat{n})$ and therefore do not radiate along the phase-matched direction $\hat{n} = \hat{k}$ where $\theta = \phi = \pi/2$. As time increases the other $M(J_D, F, q, t)$'s contribute and the radiation pattern changes.

$$\sum_{F=3}^4 \left| \sum_{q=0}^2 M(J_D = \frac{3}{2}, F, q, t) \vec{W}_q(\hat{n}) \right|^2$$

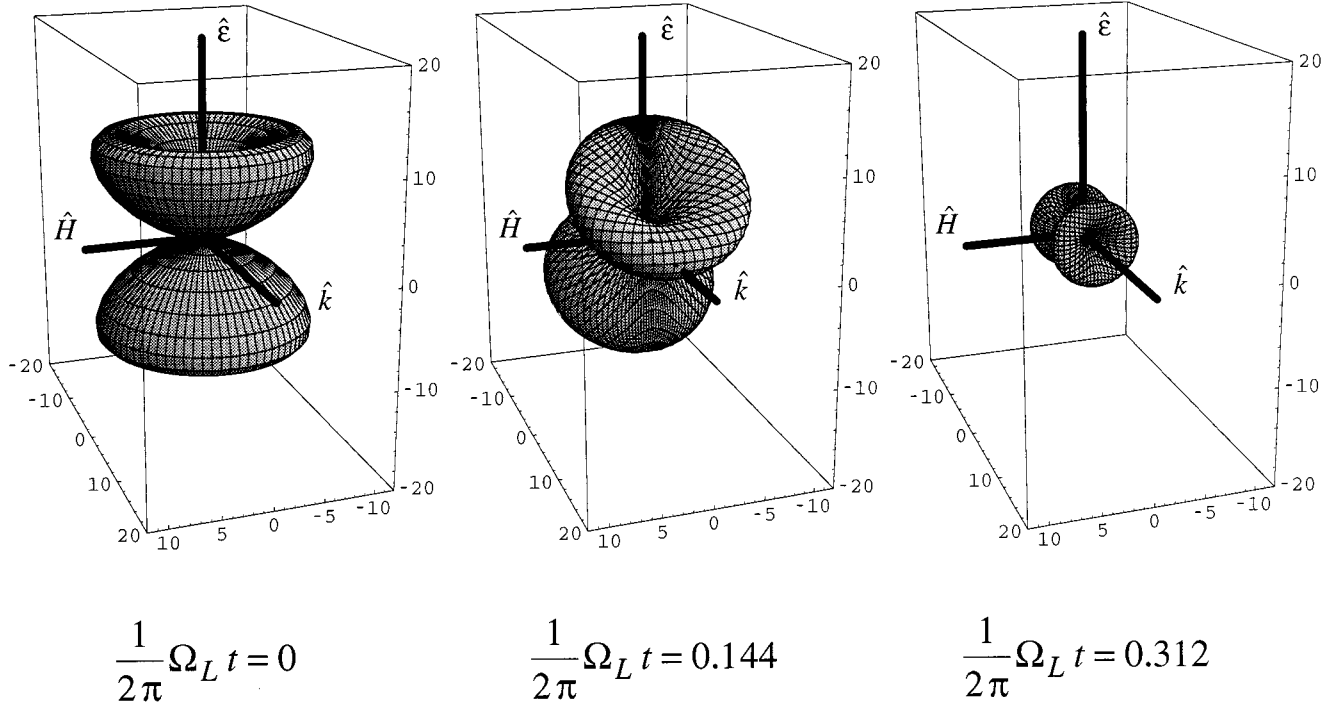


FIG. 1. Radiation patterns of an isolated atom, displayed via $\sum_{F=3}^4 |\sum_{q=0}^2 M(J_D, F, q, t) \vec{W}_q(\hat{n})|^2$ at $(1/2\pi) \Omega_L t = 0, 0.144, 0.312$ for $J_D = \frac{3}{2}$.

This change is such that radiation appears along \hat{k} to give rise to the second-harmonic emission we observe in our extended sample.

B. Evolution display

We follow the single-atom radiation pattern evolution by displaying

$$\sum_{F=3}^4 \left| \sum_{q=0}^2 M(J_D, F, q, t) \vec{W}_q(\hat{n}) \right|^2$$

at several discrete values of $(1/2\pi) \Omega_L t$ in Fig. 1. These values were chosen at successive minima and maxima of the radiated intensity along \hat{k} . We only show the radiation patterns for $J_D = \frac{3}{2}$ as the corresponding displays for $J_D = \frac{5}{2}$ are superficially identical.

The radiation pattern is initially cylindrically symmetrical about \hat{e} and zero along both \hat{e} and the plane normal to it. As time increases it appears to precess about the magnetic field while decreasing in size and distorting slightly. This precession provides a radiation component along \hat{k} , which is what we detect in our experiment. It maximizes at $\Omega_L t = 0.144$, and then at 0.312 effectively vanishes again after the radia-

tion pattern has precessed by $\pi/2$ thereby exposing the hole, initially along \hat{e} , to the \hat{k} axis. Thus the radiated component along \hat{k} modulates at four times the precessional frequency of the radiation pattern.

III. TEMPORAL EVOLUTION OF SECOND-HARMONIC EMISSION IN AN EXTENDED SAMPLE

A. Spatial interferences

In an extended sample the radiation pattern is modified by spatial interferences and so we must start with the expression for the electric field, which we write as [6]

$$\vec{E}(\vec{R}, \tau) = \frac{1}{6c^3} \int_{\text{excited volume}} (\vec{I} - \hat{n}\hat{n}) \cdot \left(\frac{d^3}{dt^3} \langle \vec{Q} \rangle_{t=\tau-1/|\vec{R}-\vec{r}|} \cdot \hat{n} \right) \times \frac{n_d(\vec{r})}{|\vec{R}-\vec{r}|} d^3\vec{r}, \quad (3.1)$$

where $\hat{n} = (\vec{R} - \vec{r}) / |\vec{R} - \vec{r}|$ and $n_d(\vec{r})$ is the density of molecules at \vec{r} . For an oscillating quadrupole moment the above expression becomes

$$\vec{E}(\vec{R}, \tau) \cong \frac{ik^3}{6} \int (\vec{I} - \hat{n}\hat{n}) \cdot \vec{Q}_{SD}(\tau) \cdot \hat{n} \times \frac{e^{ik|\vec{R}-\vec{r}|}}{|\vec{R}-\vec{r}|} n_d(\vec{r}) d^3\vec{r} + \text{c.c.} \quad (3.2)$$

In what follows it will be understood that Q is written with t replaced by τ .

Since the spatial interferences dominate, emission only occurs in a small solid angle along \vec{k} . In the far-field approximation $\hat{n} \cong \hat{k}$; since $\vec{W}_0(\hat{k}) = \vec{W}_2(\hat{k}) = 0$ we find that $(\vec{I} - \hat{n}\hat{n}) \cdot \vec{Q}_0(t) \cdot \hat{n} \cong Q_0^{2,1}(t) \vec{W}_1(\hat{k})$. Far from the sample $|\vec{k}|\vec{R} - \vec{r}| \cong kR - k\hat{n} \cdot \vec{r}$ and we write

$$\vec{E}(\vec{R}, \tau) = \frac{ik^3 \vec{W}_1(\hat{k})}{6R} e^{ikR} \int Q_{SD}^{2,1} e^{-ik\hat{n} \cdot \vec{r}} n_d(\vec{r}) d^3\vec{r} + \text{c.c.} \quad (3.3)$$

It is convenient to display the spatial and phase character of the excitation pulse $[\rho_0$ in Eq. (2.9) should have been written with the factor $e^{i\vec{k} \cdot \vec{r}}$ where $\vec{k} = 2\pi/\lambda_{\text{laser}}/2$, to account for the variation in spatial phase introduced by the excitation pulse] by writing

$$\langle Q^{2,1} \rangle = \langle Q^{2,1} \rangle_{\Theta = \pi/2} \sin \Theta(\vec{r}) e^{i\vec{k} \cdot \vec{r}} \quad (3.4)$$

so that the radiated intensity is

$$\vec{S}(\hat{n}) = \frac{c}{4\pi} |\vec{E}(\vec{R}, \tau)|_{\text{avg}}^2 \hat{n} = S_0(\hat{k})_{\Theta = \pi/2} |G(\hat{n})|^2 \hat{n}, \quad (3.5)$$

where

$$G(\hat{n}) = \int e^{i(\vec{k} - k\hat{n}) \cdot \vec{r}} \sin \Theta(\vec{r}) n_d(\vec{r}) d^3\vec{r}. \quad (3.6)$$

The radiated power is then

$$P = S_0(\hat{k})_{\Theta = \pi/2} \int |G(\hat{n})|^2 R^2 d\sigma, \quad (3.7)$$

where the integral is over the solid angle.

For a uniformly irradiated cylindrical sample of constant number density, length L , radius w_0 , and large Fresnel number

$$G(\hat{n}) = n_d \sin \Theta \int e^{ikw_0 \sin \psi \cos \xi} dL w dw d\xi, \quad (3.8)$$

where we have introduced the cylindrical coordinate w and written $\vec{k} - k\hat{n} \cong k\hat{g} \sin \psi$, where $\hat{g} \cdot \vec{k} \cong 0$, $\hat{k} \cdot \hat{n} = \sin \psi$, and $\hat{g} \cdot \vec{r} = w \cos \xi$. Writing $N = \pi n_d L w_0^2$, then on integration

$$G(\hat{n}) = 2N \sin \Theta \frac{J_1(kw_0 \sin \psi)}{kw_0 \sin \psi}, \quad (3.9)$$

(J_1 denotes Bessel's function of order 1), in which we set $\sin \psi = \psi$ and use $d\sigma = 2\pi \psi d\psi$ to obtain:

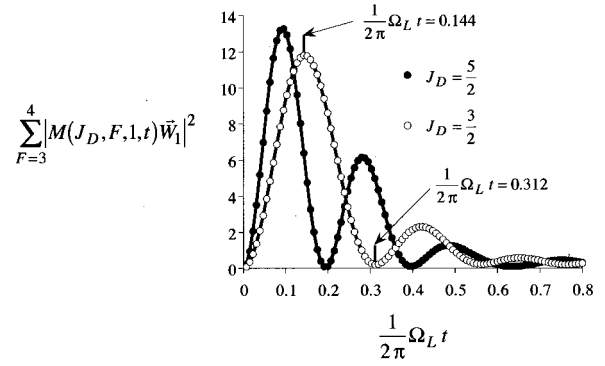


FIG. 2. Evolution of the radiated power along the phase-matched direction $\hat{n} = \hat{k}$, displayed via $\sum_{F=3}^4 |M(J_D, F, 1, t) \vec{W}_1(\hat{k})|^2$ plotted as a function of $(1/2\pi) \Omega_L t$ for both $J_D = 5/2$ and $3/2$.

$$P = N^2 \frac{\lambda^2}{\pi w_0^2} \sin^2 \Theta R^2 S_0(\hat{k})_{\Theta = \pi/2}, \quad (3.10)$$

which is the equivalent of Eq. (C6) in [11]. Substituting for $S_0(\hat{k})_{\Theta = \pi/2}$

$$P(J_D, t) = \frac{1}{72} N^2 \frac{ck^4}{w_0^2} Q_0^2 \rho_0^2 \sin^2 \Theta \times \sum_{F=3}^4 |M(J_D, F, 1, t) \vec{W}_1(\hat{k})|^2, \quad (3.11)$$

which can be written as

$$P(J_D, t) = \frac{5}{6} \frac{N^2}{k^2 w_0^2} \frac{\hbar \omega}{T_1^{SD}} \rho_0^2 \sin^2 \Theta \times \sum_{F=3}^4 |M(J_D, F, 1, t) \vec{W}_1(\hat{k})|^2, \quad (3.12)$$

where T_1^{SD} is the fluorescence lifetime of the D state for quadrupole emission to the S state. It relates to Q_0 via $1/T_1^{SD} = \frac{1}{60} (k^5/\hbar) Q_0^2$; see (6⁴⁷) in [12].

The temporal evolution of $\sum_{F=3}^4 |M(J_D, F, 1, t) \vec{W}_1(\hat{k})|^2$ is displayed in Fig. 2. Markers have been placed at $\Omega_L t = 0.144, 0.312$, where the radiation patterns were shown in Fig. 1. We note that the behavior displayed here differs from a simple precession as the ratio $0.144/0.312 = 2.2 \neq 2$ and the null at 0.312 is not complete; the “intensity” there is $0.2 \neq 0$.

For Cs, a rough estimate of the position τ_1 of the first peak is obtained by setting $J_D \omega_{J_D} \tau_1 = \pi/2$, where $J_D \omega_{J_D}$ is the highest frequency component in the radiation response.

Since the response functions of Fig. 2 depend only on $\Omega_L t$, they are universal and independent of the magnetic field. However, Doppler broadening modifies the response with time and gives rise to an H -dependent reshaping.

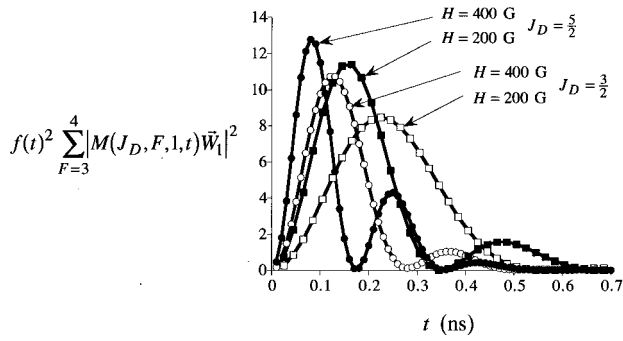


FIG. 3. Evolution of the radiated power along $\hat{n} = \hat{k}$ as degraded by Doppler dephasing, displayed via $f(t)^2 \sum_{F=3}^4 |M(J_D, F, 1, t) \tilde{W}_1(\hat{k})|^2$ plotted as a function of t in nano-seconds for both $J_D = 5/2$ and $3/2$. Separate plots are given for two fields, 200 and 400 G. In calculating $f(t)$ we have set $T_2^* = 0.52$ ns.

B. Doppler broadening

In the case of a Doppler-broadened gas the radiated power is degraded by an additional factor $f(t)^2$ so that

$$P(T, J_D, t) = f(t)^2 P(J_D, t) \quad (3.13)$$

where

$$f(t) = e^{-(\pi/4)(t/T_2^*)^2}, \quad (3.14)$$

$T_2^* = (1/k) \sqrt{\pi M / 2k_B T}$, T is the temperature, k_B is Boltzmann's constant, and M is the mass of the cesium atom. At $T = 180$ °C, $T_2^* \approx 0.53$ ns. Even though we work at relatively low temperatures and the Cs atoms are heavy, the degradation can be pronounced, as shown in Fig. 3. Here the response is plotted as a function of time in order to demonstrate the practical effect of applying a magnetic field. At 200 G the coherence is severely damped and is effectively wiped out in less than 1 ns. At 800 G the distortion is less severe since the signal is mostly over before Doppler dephasing becomes effective.

In the absence of Doppler dephasing the peak delays are inversely proportional to the magnetic field since $\omega_{1/2}, \omega_{3/2}, \omega_{5/2} \propto H$. With Doppler dephasing this proportionality fails. The degradation factor drastically shifts the peak position as its unperturbed location moves into the middle hundred picosecond region where $f(t)^2$ is significantly reduced from unity. In the low-field limit the second-harmonic response follows $t^2 e^{-(\pi/2)(t/T_2^*)^2}$, yielding a delay $\sqrt{2/\pi} T_2^* \approx 0.42$ ns independent of both J_D and H .

IV. EXPERIMENTS

A. Practical considerations

Second-harmonic radiation from the $6D_{3/2} - 6S_{1/2}$ and $6D_{5/2} - 6S_{1/2}$ transitions in Cs vapor occurs at 4427 Å and 4419 Å, respectively; see Fig. 4. But for this to happen the associated $6D$ state must be populated, which then makes possible electric-dipole transitions to the lower-lying $7P$ and $6P$ states. Since these states are initially unpopulated, superfluorescence can (and will) develop and consequently evolu-

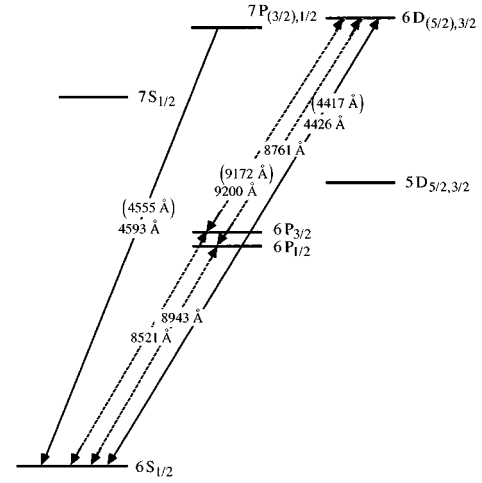


FIG. 4. Energy-level diagram highlighting the 4426-Å (4417-Å) second-harmonic transitions between the $6S_{1/2}$ and $6D_{(5/2),3/2}$ levels and the nearby yoked superfluorescence transitions at 4593 Å (4555 Å) between the $6S_{1/2}$ and $7P_{(3/2),1/2}$ levels. Also highlighted are the yoked superfluorescence transitions via the intermediate $6P$ states.

tion of the second-harmonic signal will be modified by the superfluorescence induced depopulation of the $6D$ state. Fortunately, superfluorescence does not develop until the gain αL (where α is the gain per unit length and L is the sample length) on their associated transitions becomes of the order of 100. Before then, only amplified spontaneous emission competes and its effect is not appreciable. Since αL is proportional to the excited-state population $N \sin \Theta/2$ while the second-harmonic intensity is proportional to $(N \sin \Theta/2 \cos \Theta/2)^2$, it follows that while increasing the number density to enhance the second-harmonic output, proper care has to be taken to keep the excitation energies low enough to avoid superfluorescence effects.

Another limitation on the number density comes from the requirement (implicitly assumed in our analysis) that the sample is optically thin at the second-harmonic transition. This condition is necessary to avoid depletion of the excited state due to radiation reaction [13]. In other words, the number of photons in the second-harmonic pulse should be much smaller than the number of atoms in the sample.

B. Apparatus

1. Optical circuit

Our experimental setup was almost exactly the same as described in [1]. A Spectra-Physics series 3000 actively mode-locked Nd:YAG laser (where YAG denotes yttrium aluminum garnet) was used to produce a train of 80-ps pulses separated by 12 ns. The pulse train was frequency doubled to 532 nm in a potassium dihydrogen phosphate crystal; the average output power was 1 W. After attenuation by a factor of 2 the pulses were used to synchronously pump a Spectra-Physics 375B dye laser, which was tuned to either the 885.4-nm or 883.7-nm wavelength according to which $6D_{3/2} - 6S_{1/2}$ or $6D_{5/2} - 6S_{1/2}$ two-photon transition we wanted to excite. This laser produced a train of 10-ps pulses that were close to transform limited. These pulses were then spectrally filtered [14], amplified in a Quanta-Ray pulsed dye

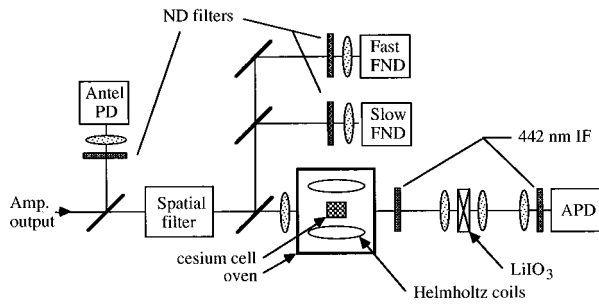


FIG. 5. Schematic diagram of apparatus. Helmholtz coils produced pulsed magnetic fields up to 1200 G. The “Antel” photodiode provided the oscilloscope trigger, the “slow FND” monitored pump energy, the “fast FND” generated a reference for eliminating jitter from the oscilloscope trigger circuits, and the “APD” registered the SH signal. Detector response was accounted for by referencing the SH generated by the Cs to that generated by the LiIO_3 crystal. When using the LiIO_3 , the magnetic field was not turned on and both interference filters were placed behind the LiIO_3 crystal.

amplifier, spatially filtered, and divided into three parts; see Fig. 5. One part was directed into an EG&G FND-100 (“slow FND”) photodiode that measured the pump pulse energy. A second part was directed onto a 1-GHz-bandwidth EG&G C30971E silicon photodiode (“fast FND”) to provide a stable time reference signal. A third part was imaged, by a 500-mm focal length achromat lens, at the center of 1-cm-thick quartz cell containing saturated cesium vapor. The cell was situated in an oven and at the center of a pair of 6-cm-diam Helmholtz coils. These coils, driven by a 250- μs period switched L - C circuit, provided an effectively static, vertically directed magnetic field. The magnetic-field module was calibrated by inducing emf in a secondary coil of known geometry, which was inserted between the Helmholtz coils in place of the cell.

Second-harmonic (SH) radiation at 442 nm, emerging from the cell along the direction of the pump, was focused on a 1-GHz-bandwidth EG&G C30921E avalanche photodiode (APD). When observing the SH emission, all radiation except the SH was blocked from entering the detector by two Andover 100 \AA full width at half maximum, 442-nm center bandpass interference filters (IF’s). At the same time, the interference filters had large enough bandwidth to serve equally well for both $6D_{3/2}-6S_{1/2}$ and $6D_{5/2}-6S_{1/2}$ transitions.

The LiIO_3 crystal placed in the telescope was used to provide a reference delay when the preceding interference filter was removed to allow the pump to activate it; otherwise it had no effect. The time-delay calibration required using the instantaneous SH from the crystal in place of the laser pump pulse because of the variation in the temporal response of the APD with the wavelength of incident light [15]. The C30921 APD is constructed of four layers of differently doped silicon. Photoelectrons are produced in the first layer by incident light and then accelerate to the highly doped third layer where current amplification occurs. The absorption depth of light in silicon varies strongly with wavelength, from 1 μm at 400 nm to 70 μm at 900 nm. By the longitudinal geometry of the APD, the photoelectrons generated by shorter-wavelength light have farther to travel to the gain region than those produced by longer-wavelength light and

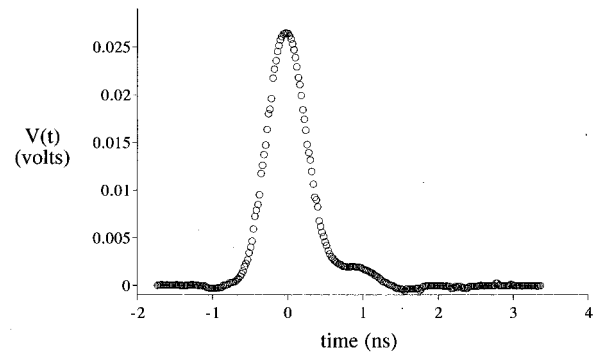


FIG. 6. Avalanche detector response to the 10-ps “instantaneous” second harmonic generated by the LiIO_3 .

the former response is delayed relative to the latter. This is the reverse of what obtains with a photomultiplier.

The outputs of the fast FND and APD’s were fed into a 1-GHz Tektronix 7A29 amplifier mounted in a Tektronix 7104 oscilloscope mainframe. The Tektronix 7B15 time base was triggered externally by the response to the pump pulse of a 35-ps rise-time Antel AR-S2 (“Antel”) photodiode. A Tektronix DCS01 digitizing camera captured oscilloscope traces with 20-ps pixel resolution. The response of the fast FND provided a time reference for each SH pulse measured by the APD, effectively eliminating oscilloscope trigger jitter from the determination of delay.

The location and cabling of the fast FND and APD were such that they produced distinct traces, separated by 3 ns, on the oscilloscope screen whose time base was set to 1 ns per division. The connection between the displayed time interval and the actual time delay between the pump and Cs SH pulses was made by making a separate measurement in which an instantaneous SH pulse was substituted for the Cs SH pulse. This was done by (i) turning off the magnetic field and (ii) removing the IF filter that preceded the telescope containing the 1-mm-thick LiIO_3 crystal near its focal point. In the absence of a magnetic field no Cs SH is produced and the focused pump pulse at the LiIO_3 crystal generates a short SH pulse with no measurable delay. Here as elsewhere the position of a SH pulse is defined by the location of its intensity peak. By pulse delay we mean peak delay.

2. Detector response

The overall APD detector-oscilloscope response $V(t)$ to the 10-ps laser pulse at the second-harmonic (generated by the LiIO_3 crystal) is displayed in Fig. 6. It is significantly longer than 10 ps and, in addition, exhibits ringing. The distortion it introduces is considerable; however, when convoluted with $P(T, J_D, t)$ of Eq. (3.13) it provides an adequate reference for comparison with experiment:

$$I_{\text{det}}(t) = \int P(T, J_D, t') V(t-t') dt'. \quad (4.1)$$

The correction in the determination of the (peak) delay introduced by taking into account the detector response is quite dramatic as can be seen by comparing the (peak) delay curves Figs. 7 and 8 for $J_D=3/2$ and $J_D=5/2$, respectively. In each figure, the dashed curve includes the detector re-

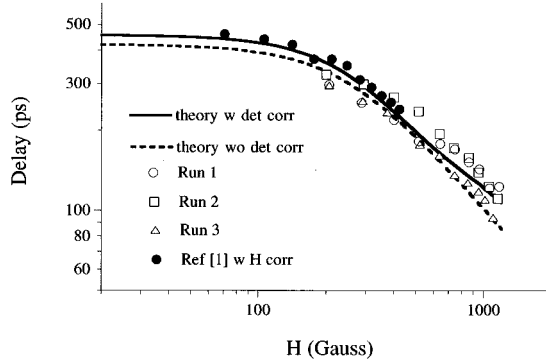


FIG. 7. Comparison of experimental and theoretical (both with and without accounting for the detector response function) delays in the second-harmonic emission on the $6S_{1/2}-6D_{3/2}$ transition as functions of magnetic field.

response; the solid curve does not. Note that the slope of each solid curve is -1 at large fields and levels off (to zero) at low fields to a value independent of J_D in accord with our discussion in, and immediately preceding, Sec. III B.

Including the detector response increases the (peak) delay in proportion to the temporal width of the uncorrected response. In the limit of small H the corrected response is ≈ 30 ps greater and again independent of J_D as the response curves become independent of J_D as $H \rightarrow 0$. As the field increases the “low-field” response width first narrows and the associated additional delay gets smaller. Next, the effective width broadens as the ringing in the response (see Fig. 2) is no longer hidden by Doppler dephasing. For $J_D = 5/2$ these effects come into play sooner as H is increased.

3. Delay measurements

For each value of the magnetic field, 100–150 wave-form traces were recorded. Each trace consisted of the pump pulse followed by the SH pulse. There was considerable variation in the absolute and relative sizes of the two traces and the first pulse could effect the shape of the second if it were sufficiently more intense. Our setup was such that if we ignored all wave-form traces exceeding 20 MV this effect was negligible. At the other end we ignored wave-form traces

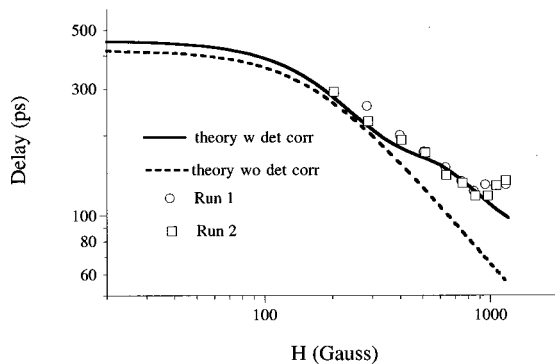


FIG. 8. Comparison of experimental and theoretical (both with and without accounting for the detector response function) delays in the second-harmonic emission on the $6S_{1/2}-6D_{5/2}$ transition as functions of magnetic field.

below 5 MV since thermal noise then became destructive. The overall effect of this selection process was to remove 50–80% of the recorded traces. This was sufficient for the purpose of the experiment as after averaging, the error in the value of pulse peak separations was dominated by the 20 ps per pixel camera resolution.

4. Sample cell

All experiments were performed in a quartz cell. Although the previous work [1] was performed in both quartz and stainless-steel cells, the signals from the quartz cell were of poor quality and only the results from the much longer stainless-steel cell were analyzed in any detail. This was unfortunate inasmuch as eddy currents from the applied pulsed magnetic field reduced the field at the sample by about a factor of 0.36 and prevented a suitable comparison between experiment and theory.

5. Energy measurements

We have also checked our calculation of the emitted SH power (3.13) by measuring the total energy of the SH pulse

$$\mathcal{E}_{\text{SH}} = \int P(T, J_D, t) dt. \quad (4.2)$$

Our object here was to determine both the absolute magnitude of the SH response as well as the functional dependence of the SH energy on the excitation pulse energy. We replaced the avalanche photodetector with the slower but more sensitive RCA C31034 photomultiplier tube. The photomultiplier output as well as the slow FND detector (to provide the excitation energy) were directed into Stanford Research Systems SR250 gated integrators. Their gate widths were set at 40 ns to amply cover each pulse and the outputs were separately stored in a computer without any averaging. C31034 photomultiplier tubes vary in gain, from one tube to the next, by more than an order of magnitude and so we calibrated ours by looking at the anode current resulting from a “typical” single photoelectron. At the 1.5-kV bias the measured gain was 3×10^6 , which is at the upper end of the gain distribution for these tubes [16]. Since the excitation intensity fluctuated considerably, the dependence of the SH energy \mathcal{E}_{SH} over a wide range of pump pulse energies $\mathcal{E}_{\text{pump}}$ could be obtained by collecting data at a single setting of the laser system.

C. Results

1. Delay

Measurements of second-harmonic delay for experiments performed on the $6S_{1/2}-6D_{3/2}$ and $6S_{1/2}-6D_{5/2}$ transitions in a quartz cell at 170 °C are presented in Figs. 7 and 8, respectively. The open markers denote data sets taken on different days. For comparison we also present, in the form of solid circles, the data from Ref. [1], except that the magnetic-field values reported there have all been reduced by a factor of 0.36. This is the reduction we ascribe as due to the induction of eddy currents by the application of the pulsed magnetic field. It was determined by simply fitting to the open circle data. With this correction all data are in agreement. The de-

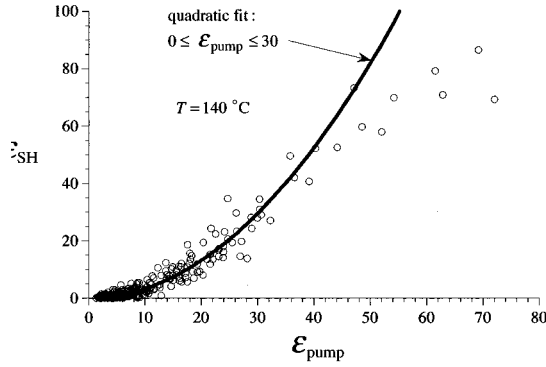


FIG. 9. Second-harmonic energy displayed as a function of pump energy at $T=140^\circ\text{C}$ and $H=290\text{ G}$. The initial dependence of \mathcal{E}_{SH} on $\mathcal{E}_{\text{pump}}^2$ is displayed by the quadratic fit.

tector response correction was clearly essential in analyzing the $J_D=5/2$ data, only marginally so for $J_D=3/2$.

Some data sets are displaced from each other by a fixed amount we ascribe to the difficulty in determining, by better than 20 ps, the reference value of the pump-SH peak separation associated with undelayed SH generation. Since this value is determined once for each run and then subtracted from all pump-SH peak separation data the whole data set can be shifted by 20 ps. In addition, there is an uncertainty of 20 ps in the determination of the Cs SH delay for each particular data point.

2. Energy

(a) *Functional dependence.* The excitation pulse area Θ should vary in proportion to the pump energy $\mathcal{E}_{\text{pump}}$ since second-harmonic generation is a second-order process. For low pump powers $\sin \Theta \sim \Theta$ and we then expect that the \mathcal{E}_{SH} should vary as $\mathcal{E}_{\text{pump}}^2$. To verify this, a number of $\mathcal{E}_{\text{SH}}, \mathcal{E}_{\text{pump}}$ data sets were obtained at temperatures ranging from 140°C to 220°C . The expected quadratic dependence was indeed observed at low pump intensities. It then broke off at an energy $\mathcal{E}_{\text{pump}}^{\text{br}}$ (Fig. 9), which was found to decrease with temperature. Measurements of the $7P-6S$ superfluorescence energies \mathcal{E}_{SF} performed for the same range of temperatures showed that $\mathcal{E}_{\text{pump}}^{\text{br}}$ was approximately the same as the threshold pump energy for the superfluorescence (Fig. 10). It can thus be concluded that it is the onset of superfluorescence that causes the quadratic dependence of \mathcal{E}_{SH} on $\mathcal{E}_{\text{pump}}$ to fail.

The measurements summarized in Fig. 11 display the initial quadratic slope as obtained from each of a set of experiments performed at five different temperatures. A straight line of slope 2 has been drawn through the data points to show the agreement with the expected dependence of the energy on n_d^2 .

(b) *Magnitude.* The maximum second-harmonic signal observed at $T=180^\circ\text{C}$ corresponds to 2×10^6 photons referred back to the sample. This value was effectively independent of magnetic field over a range 300–1200 G. The sample length was 1 cm with the beam radius at which the intensity is reduced by $1/e$, of about 0.03 cm. At the specified sample temperature there were $N=2 \times 10^{12}$ Cs atoms in the cylindrical volume determined by the noted radius and

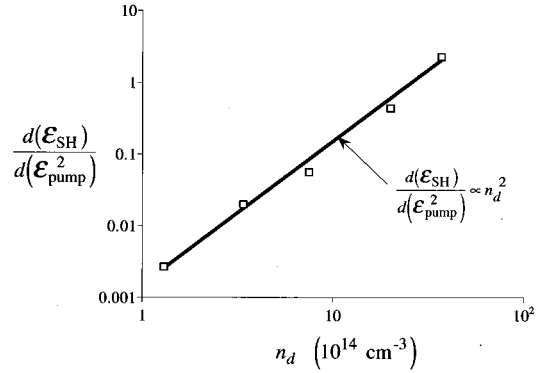


FIG. 10. Second-harmonic and superfluorescence pulse energies displayed as functions of pump energy. The superfluorescence threshold is clearly displayed. All measurements were made at $H=290\text{ G}$.

length. Integrating Eq. (3.13) over time with $T_1^{SD}=(2 \times 10^6)T_1^{SP}$ [17], $T_1^{SP}=30 \times 10^{-9}\text{ s}$, and

$$\int_0^\infty f(t)^2 \sum_{F=3}^4 |M(J_D, F, 1, t) \vec{W}_1(\hat{k})|^2 dt \approx 2\text{ ns} \quad (4.3)$$

for both $J_D=3/2$ and $5/2$ (see Fig. 3), we estimate the number of photons radiated by the sample at $T=180^\circ\text{C}$ to be $2 \times 10^7 \sin^2 \Theta$. This result validates our assumption that the sample is optically thin.

If we set $\Theta = \pi/10$ we obtain the experimentally measured result. For an independent estimate of Θ we examine Fig. 9. At $T=140^\circ\text{C}$ it shows that the quadratic dependence of \mathcal{E}_{SH} on $\mathcal{E}_{\text{pump}}$ continues until $\mathcal{E}_{\text{pump}} \approx 40$. This means that at $\mathcal{E}_{\text{pump}} \approx 40$ the pulse area is still small enough for the approximation $\sin \Theta \approx \Theta$ to stay valid, i.e., $\Theta(\mathcal{E}_{\text{pump}}=40) \leq \pi/4$. But our measurements were made at $T=180^\circ\text{C}$ where superfluorescence begins at $\mathcal{E}_{\text{pump}} \approx 25$. Noting that the dependence of Θ on $\mathcal{E}_{\text{pump}}$ is independent of temperature; we conclude that $\Theta \leq \pi/7$.

The close agreement obtained is clearly fortuitous. Our calculation has assumed the excitation beam to be uniform when in fact it has a Gaussian profile. The notion of a single Θ throughout the excited volume is not, strictly speaking,

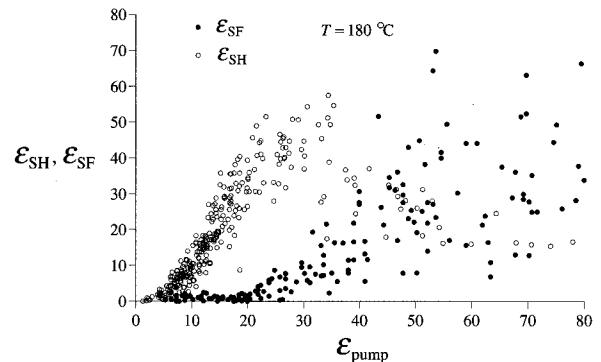


FIG. 11. Derivative of the second-harmonic energy with respect to the square of the pump energy, displayed for several values of n_d . All measurements were made at $H=290\text{ G}$.

correct. Our analysis, though rough, is good enough to enable us to claim that we understand the origin and magnitude of the observed SH signals.

V. CONCLUSIONS

The discrepancy between theory and experiment in [1] has been resolved by taking into account the screening of the applied magnetic field inside a nonmagnetic 304-type stainless-steel cell by pulse-induced eddy currents. The field at the cell was produced by a 250- μ s period single sine wave current pulse applied to a Helmholtz coil and was sufficiently short to induce shielding currents that reduced the applied field by a factor of 2–3.

In addition to the second-harmonic measurements made on the $6D_{3/2}$ - $6S_{1/2}$ transition in [1], we have studied the second-harmonic delay behavior of the $6D_{5/2}$ - $6S_{1/2}$ transi-

tion. Here we find similar but distinct behavior and again obtain agreement between theory and experiment after taking into account the short-pulse response of the APD detector. This latter consideration was not essential in the first experiment, but very important in the second.

The intensity behavior of the second-harmonic signal versus pump intensity exhibited quadratic character as long as the latter did not exceed a certain limit after which a superfluorescent burst occurred [18], depleting the population of the upper $6D$ level and knocking down the second-harmonic signal. The quadratic slope of the aforementioned dependence was proportional to the second power of the number density in agreement with the theory of cooperative phenomena. The total energy of the second-harmonic pulse was found to be in good agreement with what was theoretically expected.

-
- [1] J. H. Brownell, X. Lu, and S. R. Hartmann, *Phys. Rev. Lett.* **75**, 3657 (1995).
- [2] J. A. Armstrong, N. Bloembergen, J. Bucuing, and P. S. Pershan, *Phys. Rev.* **127**, 1918 (1962).
- [3] A. Flusberg, T. Mossberg, and S. R. Hartmann, *Phys. Rev. Lett.* **38**, 59 (1977).
- [4] A. Flusberg, T. Mossberg, and S. R. Hartmann, *Phys. Rev. Lett.* **38**, 694 (1977).
- [5] M. Matsuoka, *Resonances* (World Scientific, Singapore, 1990), 104–111.
- [6] L. D. Landau and E. M. Lifshitz, *The Classical Theory of Fields* (Pergamon, Oxford, 1975).
- [7] S. R. Hartmann, *IEEE J. Quantum Electron.* **QE-4**, 802 (1968).
- [8] H. Kopfermann and E. E. Schneider *Nuclear Moments* (Academic, New York, 1958).
- [9] C. Tai, W. Happer, and R. Gupta, *Phys. Rev. A* **12**, 736 (1975).
- [10] N. Ph. Georgiades, E. S. Polzik, and H. J. Kimble, *Opt. Lett.* **19**, 1474 (1994).
- [11] I. D. Abella, N. A. Kurnit, and S. R. Hartmann, *Phys. Rev.* **141**, 391 (1966).
- [12] E. U. Condon and G. H. Shortley, *The Theory of Atomic Spectra* (Cambridge University Press, New York, 1957).
- [13] R. Friedberg and S. R. Hartmann, *Phys. Lett.* **37A**, 285 (1971).
- [14] X. Lu, J. H. Brownell, and S. R. Hartmann, *Opt. Commun.* **120**, 295 (1995).
- [15] J. H. Brownell, Ph.D. thesis, Columbia University, 1995 (unpublished).
- [16] Burle Industries, Inc., Tube Products Division, Lancaster, PA (private communication).
- [17] W. Prokofjew, *Z. Phys.* **57**, 387 (1929).
- [18] J. H. Brownell, X. Lu, and S. R. Hartmann, *Phys. Rev. Lett.* **75**, 3265 (1995).